



A phytoplankton bloom caused by the super cyclonic storm Amphan in the central Bay of Bengal

Haojie Huang^{1,4}, Linfei Bai^{3,4}, Hao Shen⁴, Xiaoqi Ding^{3,4}, Rui Wang^{3,4}, and Haibin Lü^{1,2,4}

¹Jiangsu Key Laboratory of Marine Bioresources and Environment/Jiangsu Key Laboratory of Marine Biotechnology, Jiangsu Ocean University, Lianyungang, Jiangsu Province, China

²Co-Innovation Center of Jiangsu Marine Bio-industry Technology, Jiangsu Ocean University, Lianyungang, Jiangsu Province, China

³Lianyungang Meteorological Bureau, Lianyungang, Jiangsu Province, China

⁴School of Marine Technology and Geomatics, Jiangsu Ocean University, Lianyungang, Jiangsu Province, China

Correspondence: Haibin Lü (haibin_lv@jou.edu.cn)

Received: 21 April 2023 – Discussion started: 26 April 2023

Revised: 12 July 2023 – Accepted: 17 July 2023 – Published: 16 August 2023

Abstract. The super cyclonic storm Amphan originated in the central Bay of Bengal (BoB) in May 2020, and a phytoplankton bloom occurred in the upper ocean that was devoid of background nutrients. The dynamic mechanism of the chlorophyll *a* (Chl *a*) bloom was researched based on re-analysis data, remote sensing and Argo float data. During the passage of Amphan, an inertial oscillation with a 2 d period appeared in the thermocline and lasted for approximately 2 weeks. After the passage of Amphan, a cyclonic eddy with a maximum vorticity of approximately 0.36 s^{-1} formed in the study area (Box A). Additionally, horizontal transport of Chl *a* also occurred when the maximum inlet fluxes through the western and northern sides of Box A were 0.304 and $-0.199 \text{ mg m}^{-2} \text{ s}^{-1}$, respectively. With the weakened thermocline and thinner barrier layer thickness (BLT), nitrate and Chl *a* were uplifted to the upper ocean by upwelling. Then, with the high photosynthetically available radiation (PAR) in the upper ocean, a phytoplankton bloom occurred. This study provides new insights into the biological responses in the BoB during the passage of tropical cyclones (TCs).

trusion caused by TCs can lead to a range of ecological damage by causing land salinization and disruption of upstream freshwater systems (Mitra, 2020). Soil moisture is critical in climate evolution (Cai et al., 2017), and soil salinization can alter soil moisture and indirectly affect climate change. Additionally, internal waves have also been observed during and after TC passage, which can exert force and torque on the tendon legs of offshore oil platforms (Lü et al., 2016). Strong cyclones can also cause deformation of structures such as dams and pose a risk to undersea pipelines (Guan, 2019; Qiu, 2020). The Bay of Bengal (BoB), which has a tropical monsoon climate, is a semienclosed basin in the North Indian Ocean, which has one of the highest cyclone frequencies in the world (Vinayachandran, 2003). TCs in the BoB appear more frequently during the premonsoon (April to June) and postmonsoon (October to December) periods (Girishkumar and Ravichandran, 2012), which are 3 to 4 times more frequent than TCs in the Arabian Sea (Akter and Tsuboki, 2014). A strong saline stratification forms in the upper ocean due to the influx of freshwater from river discharge and monsoonal rainfall (He et al., 2020; Thadathil et al., 2007). Generally, TCs can cause phytoplankton blooms, thus increasing the concentration of chlorophyll *a* (Chl *a*) at the sea surface (Nayak and Rajawat, 2001; Rao et al., 2006; Vinayachandran, 2003; Zhao et al., 2015). During the passage of Phethai (Xia et al., 2022), a cyclonic eddy in eastern Sri Lanka was enhanced with a maximum vorticity of 0.36 s^{-1} , which trig-

1 Introduction

Tropical cyclones (TCs) are serious natural disasters. Heavy rainfall, storm surges and other disasters accompany TCs, resulting in huge economic losses and casualties (Girishkumar and Ravichandran, 2012; Lu et al., 2020). Rapid saltwater in-

gered a Chl *a* bloom with a maximum Chl *a* concentration of 0.6445 mg m^{-3} .

In other sea areas, after the passage of Typhoon Nuri in the western Pacific (Zhao et al., 2009), nutrient-rich water was transported from the deep layer and the coast to offshore regions, nourishing phytoplankton biomass, and then two Chl *a* patches were observed near the Pearl River Estuary and the Dongsha Archipelago. Typhoon Lupit (Cheung et al., 2012) in the northwestern Pacific also caused Chl *a* blooms. Some studies have shown that phytoplankton blooms are caused by Ekman pumping (Vinayachandran, 2003), while others have suggested that blooms are caused by cyclonic eddies (Gomes et al., 2000). In the Gulf of Mexico, a tropical sea area in the western Atlantic Ocean, after the passage of Michael in the northeastern Gulf of Mexico (Nyadjro et al., 2022), chlorophyll concentrations also significantly rose by nearly 0.7 mg m^{-3} . TC Amphan, which was the first extremely serious storm of this century, intensified from a cyclonic storm (CS) to a super cyclone within 36 h (Golder et al., 2021). TC Amphan formed over the Indian Ocean on 5 May 2020 and enhanced to a high speed. On 21 May, it made landfall along the coast of Bangladesh. A total of 4 d after the passage of Amphan, a phytoplankton bloom occurred in the central Bay of Bengal, where the upper ocean was devoid of background nutrients. Why did this phytoplankton bloom happen? However, little attention has been paid to it in this study area.

In this study, the phytoplankton bloom mechanism in the central BoB caused by TC Amphan was investigated. The data and methodology are provided in Sect. 2, followed by the results in Sect. 3, and a discussion is provided in Sect. 4. Finally, we provide our conclusions in Sect. 5.

2 Data and methods

2.1 Study area

The study area was located in the central BoB. Amphan was the costliest storm ever recorded in the BoB due to its catastrophic damage. We examined one box, named Box A ($13.5\text{--}15.5^\circ \text{ N}$, $86^\circ \text{ N--}88^\circ \text{ E}$), along the path of Amphan (Fig. 1). First, a depression formed in the southeast BoB at 9.5° N , 87.5° E on 15 May, which intensified into a deep depression in a short amount of time and further developed into a cyclonic storm the following day. Then, Amphan rapidly intensified into a super cyclonic storm with a maximum wind speed of 74.59 m s^{-1} . Finally, it steadily weakened and made landfall on 20 May.

2.2 Data

The track of TC Amphan is available from the Joint Typhoon Warning Center (JTWC; <https://www.metoc.navy.mil/jtwc/jtwc.html>, last access: 6 September 2022).

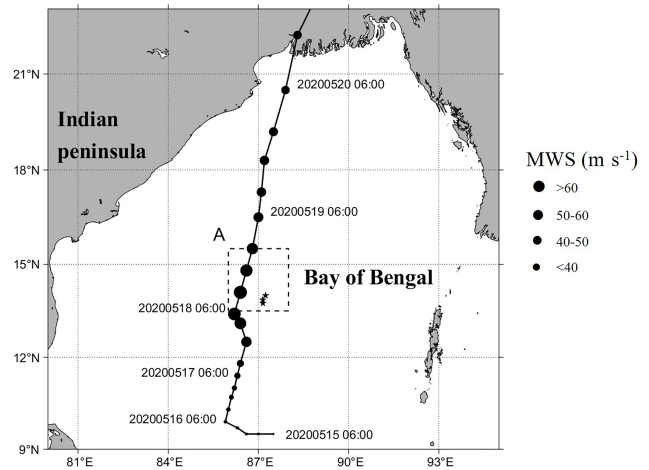


Figure 1. Track of TC Amphan. TC center locations are marked as black circles, indicated with their time in year–month–date–hour format. Locations of the Argo floats are indicated by stars (platform number 2902 769). The study area of Box A is denoted by the dashed black square: $13.5\text{--}15.5^\circ \text{ N}$, $86\text{--}88^\circ \text{ E}$. MWS signifies maximum wind speed.

Wind vector and sea surface temperature (SST) data are available from remote sensing systems (RSS; <http://www.remss.com/measurements/>, last access: 11 October 2022).

High-resolution ($0.83^\circ \times 0.83^\circ$) daily sea surface height (SSH), sea current velocity, temperature and Chl *a* data are available from the Copernicus Marine Environment Monitoring Service (CMEMS; <http://marine.copernicus.eu/>, last access: 13 September 2022).

Climatic nitrate data with a resolution of $1^\circ \times 1^\circ$ for May are accessible from the World Ocean Atlas (WOA; <https://www.ncei.noaa.gov/products/world-ocean-atlas>, last access: 18 February 2023).

Temperature and salinity profiles are accessible from the International Argo Project (<http://www.argodatamgt.org/>, accessed, last access: 4 October 2022), which began in 1999 (Gould, 2005; Jayne et al., 2017; Roemmich et al., 2009). The buoy positions in Fig. 1 are marked by stars. The Argo platform number in this study is 2 902 769.

Daily surface Chl *a* concentrations with a 4 km spatial resolution and photosynthetically active radiation (PAR) data are accessible from the satellite remote sensing of the GlobColour Project (<https://www.globcolour.info/>, last access: 12 September 2022).

The reanalyzed daily Chl *a* data with a spatial resolution of 4 km are accessible at <https://data.marine.copernicus.eu/products>. Ocean color remote sensing satellites can be used to observe chlorophyll distributions and phytoplankton blooms due to the different reflectivity of electromagnetic radiation. The chlorophyll content can be estimated by comparing the reflectance at different wavelengths (Balaguru et al., 2012; Dwivedi et al., 2008).

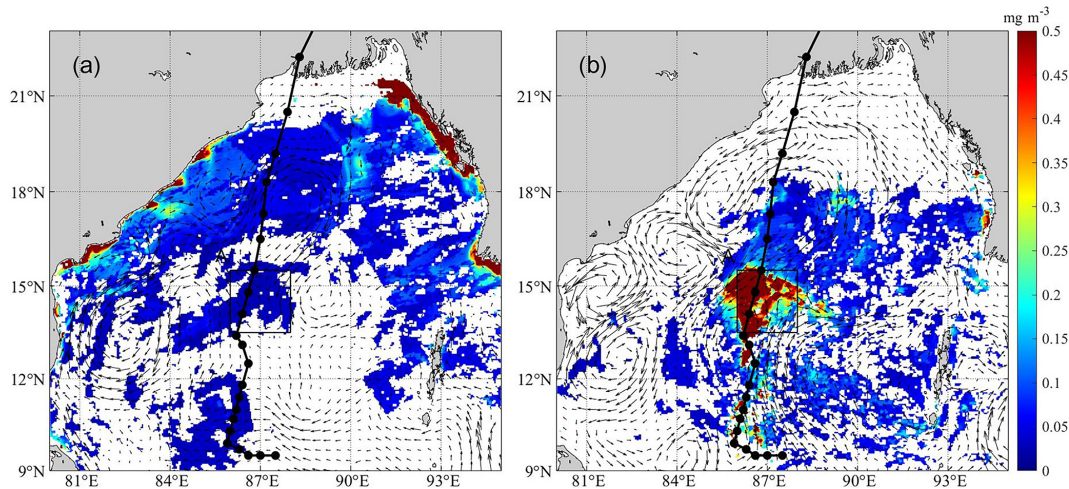


Figure 2. Surface Chl *a* concentration composited for 12–14 May (a) and 25–27 May (b). Sea surface currents are represented by black arrows.

Table 1. Information on TC Amphan (MWS: maximum wind speed).

Latitude (° N)	Longitude (° E)	Time	MWS (m s ⁻¹)	Minimum sea level pressure (mb)
9.5	87.0	2020/05/15/12	15.43	1002
9.7	86.3	2020/05/16/00	18.00	999
10.3	86.0	2020/05/16/12	25.72	992
11.0	86.2	2020/05/17/00	30.86	982
11.8	86.4	2020/05/17/12	41.15	970
13.1	86.4	2020/05/18/00	66.87	919
14.1	86.4	2020/05/18/12	74.59	901
15.5	86.8	2020/05/19/00	64.30	925
17.3	87.1	2020/05/19/12	54.01	946
19.2	87.5	2020/05/20/00	51.44	947
22.2	88.3	2020/05/20/12	48.87	954
25.2	90.1	2020/05/21/00	25.72	984

2.3 Methods

2.3.1 Ekman pumping velocity (EPV)

The vertical mixing of the upper ocean that is caused by TCs is inseparably related to Ekman pumping. Equations (1) and (2) can be used to calculate EPV (Bai et al., 2023; Gaube et al., 2013):

$$W_E = \text{Curl}(\vec{\tau} / \rho_0 f), \tag{1}$$

$$\vec{\tau} = \rho_a C_D \left| \vec{U}_{10} \right| \vec{U}_{10}, \tag{2}$$

where the Coriolis parameter f is the function of latitude θ and the earth’s rotational velocity ω , which is calculated by $f = 2\omega \sin\theta$; $\vec{\tau}$ is the wind stress; ρ_0 and ρ_a represent

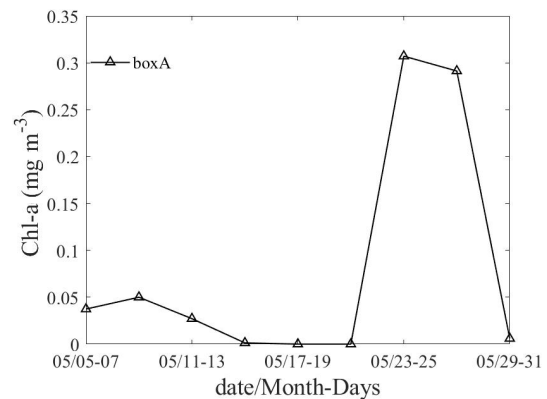


Figure 3. Time series of 3 d averaged Chl *a* concentration in Box A from 5 to 31 May.

the seawater density and the air density, respectively; C_D is the drag coefficient; and \vec{U}_{10} represents the wind speed at 10 m a.s.l. (above sea level) (Wang et al., 2010).

2.3.2 Vorticity

The curl of a sea current vector can be calculated by Eq. (3) (Lu et al., 2020):

$$\text{Curl} = dv/dx - du/dy, \tag{3}$$

where u and v are the components of sea current velocity along the x and y directions, respectively.

2.3.3 Brunt–Vaisala frequency

The Brunt–Vaisala frequency (N) can describe the stability of seawater and the atmosphere (Bai et al., 2023). It can be calculated as follows:

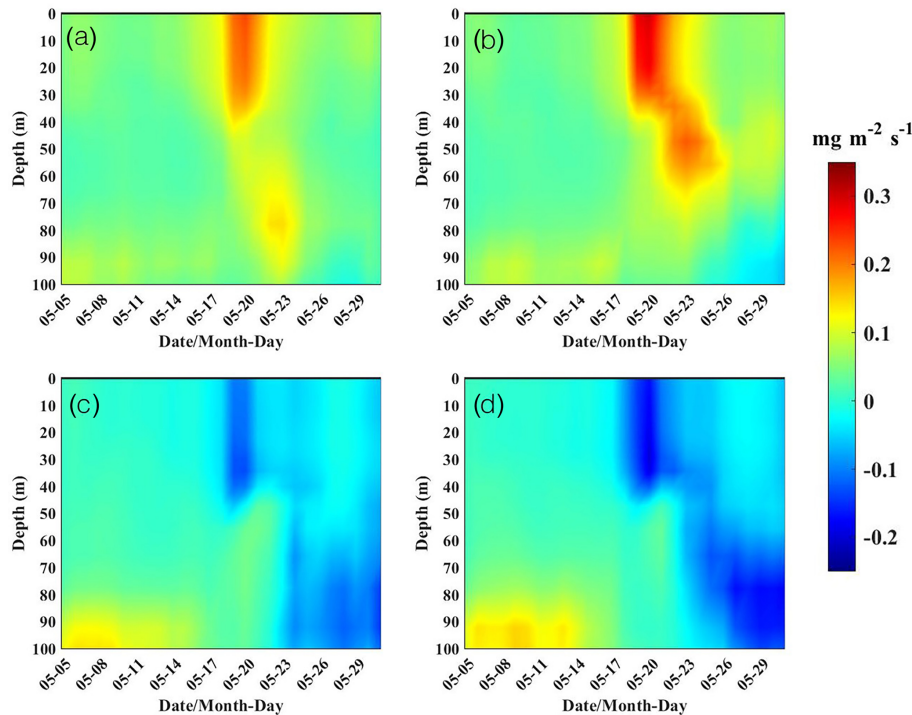


Figure 4. Time series of Chl *a* fluxes through the eastern (a), western (b), southern (c) and northern (d) sides of Box A from 5 to 31 May.

$$N = \sqrt{\frac{-g}{\rho} + \frac{d(\rho)}{d(z)}}, \quad (4)$$

where ρ is the seawater potential density, g is the gravitational acceleration and z is the vertical coordinate component. The location of the thermocline is defined at the depth of the maximum N (Lu et al., 2020).

2.3.4 Barrier layer thickness

The mixing layer depth (MLD), isothermal layer depth (ILD) and barrier layer thickness (BLT) in this study area were examined (He et al., 2020). MLD is the increase in the upper-ocean potential density ($\Delta\sigma_\theta$) when the SST decreases by 0.5°C ($\Delta T = -0.5^\circ\text{C}$) (Eqs. 5–7), the depth of the ILD is the depth (D) at which the temperature is 0.5°C lower than the SST (Eqs. 8 and 9), and the BLT is the difference between the MLD and ILD (Eq. 10):

$$\Delta\sigma_\theta = \sigma_{\text{MLD}} - \sigma_{10}, \quad (5)$$

$$\Delta\sigma_\theta = \sigma_\theta(T_{10} + \Delta T, S_{10}, P_0) - \sigma_\theta(T_{10}, S_{10}, P_0), \quad (6)$$

$$\text{MLD} = \sigma_{\text{MLD}}, \quad (7)$$

$$\Delta T = T_{\text{ILD}} - T_{10}, \quad (8)$$

$$\text{ILD} = D_{\text{ILD}}, \quad (9)$$

$$\text{BLD} = \text{ILD} - \text{MLD}, \quad (10)$$

where T_{10} and S_{10} represent the temperature and salinity at 10 m depth, separately, and P_0 represents the pressure at the sea surface.

3 Results

3.1 Amphan's path and wind field

According to the information from the India Meteorological Department, TCs can be classified by their near-center maximum wind speed (MWS), ranging from a depression (TD; $31\text{--}49\text{ km h}^{-1}$) to a super cyclonic storm (SCS; $\geq 220\text{ km h}^{-1}$). Amphan was the first and most serious cyclonic storm in May 2020. It originally appeared at 9.5°N , 87.5°E on 15 May 2020 and landed at 22.2°N , 88.3°E on 20 May 2020 (Table 1). After Amphan's formation, it generally continued to move northward along the Bay of Bengal.

3.2 Chl *a*

Bad weather conditions during the TC resulted in the poor usability of daily satellite Chl *a* data. Zhao et al. (2015) determined the Chl *a* concentration by synthesizing data for 3 d (Zhao et al., 2015). Here, we use the same method to display the Chl *a* changes in the study zone. Figure 2 displays the sea surface Chl *a* concentration composited for 12–14 and 25–27 May before and after the passage of Amphan. Figure 3 shows the 3 d averaged Chl *a* concentration over time. The Chl *a* concentration in Box A increased at an extremely high

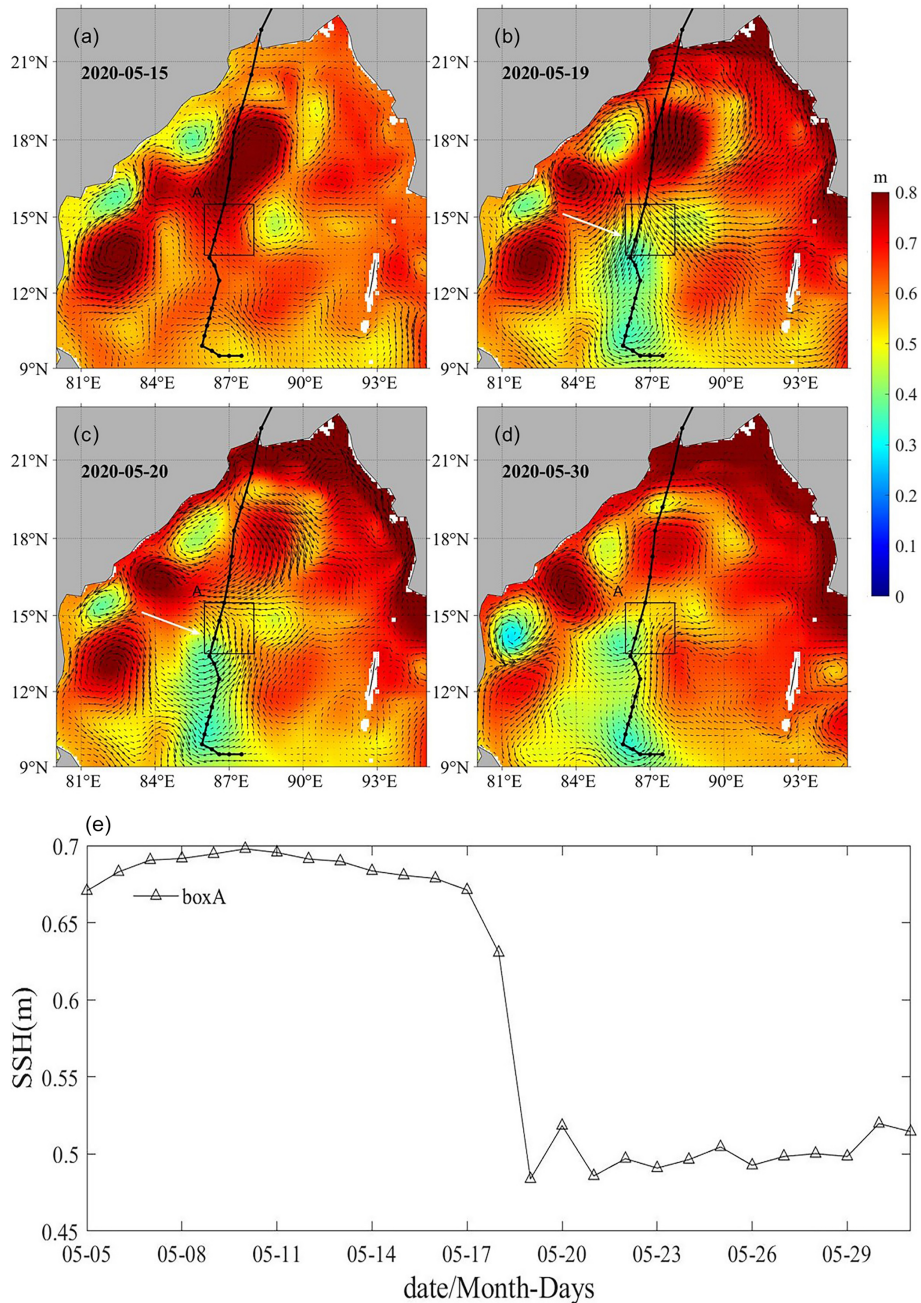


Figure 5. Sea surface current (unit in m s^{-1}) on 15 May (a), 19 May (b), 20 May (c) and 30 May (d). Time series of SSH in Box A (e). The color bar represents the SSH (unit in m). The track of Amphan is marked by the black line.

speed from 22 May until it reached a peak of 0.3071 mg m^{-3} , where the high concentration was maintained for approximately 5 d, and then it rapidly decreased on 28 May. The reasons for the Chl *a* bloom are provided below.

Figure 4 shows the Chl *a* fluxes through the southern, northern, eastern and western sides of Box A from 5 to 31 May. We can calculate the Chl *a* fluxes on the southern and northern sides by multiplying the Chl *a* concentration by *v*, and multiplying by *u* achieves the Chl *a* fluxes on the

eastern and western sides (Xia et al., 2022). Positive values and negative values represent the flow-in and flow-out on the southern and western sides, respectively; in contrast, the flux-in and flux-out on the eastern and northern sides were exactly the opposite. First, it was clearly shown that Chl *a* entered from both the western and the northern sides and discharged from the other two sides. Second, the high Chl *a* flux in the upper ocean was maintained for 4 d (Fig. 4b and d); the maximum flux from the western side was $0.304 \text{ mg m}^{-2} \text{ s}^{-1}$, and

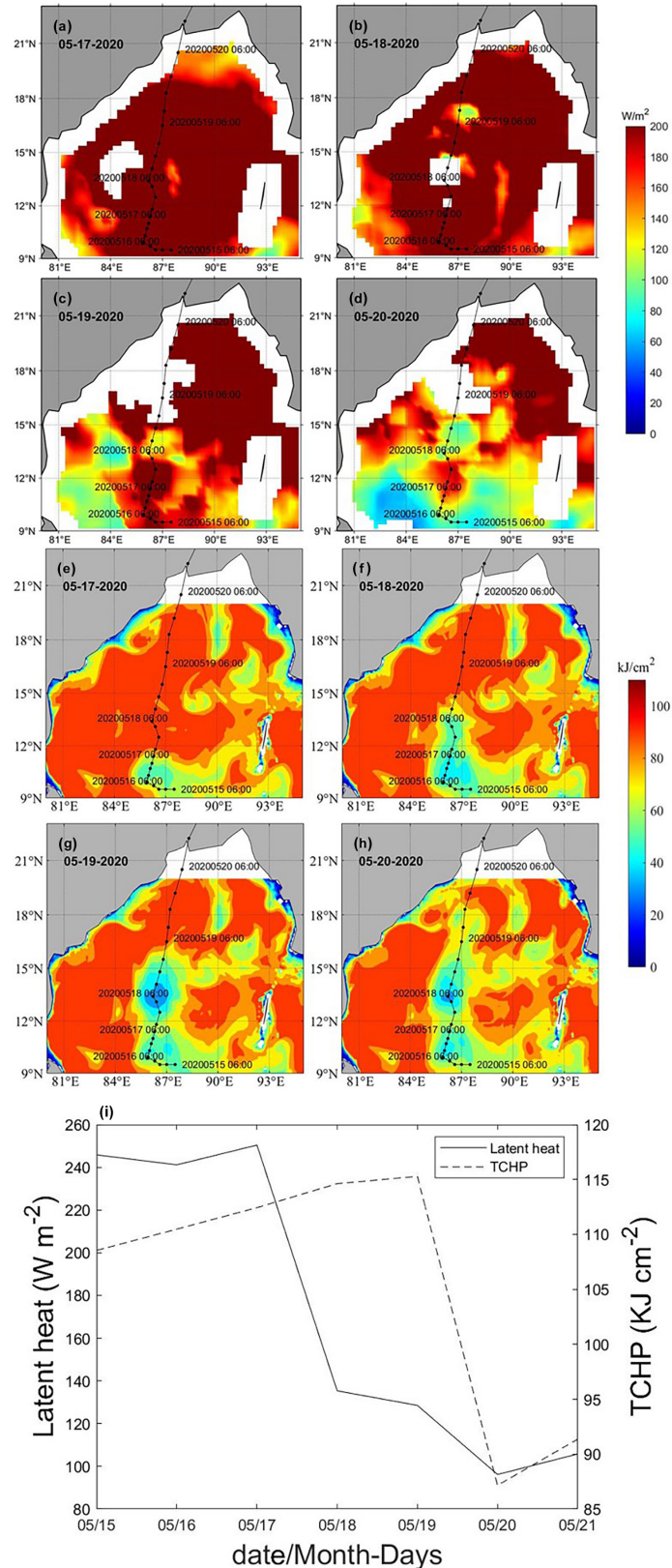


Figure 6. The ocean heat distribution during the development of the TC. Panels (a)–(d) and (e)–(h) show the variations in latent heat flux and the changes in TCHP from 17 to 20 May 2020, respectively, and *i* represents time series of mean latent heat fluxes and TCHP in Box A.

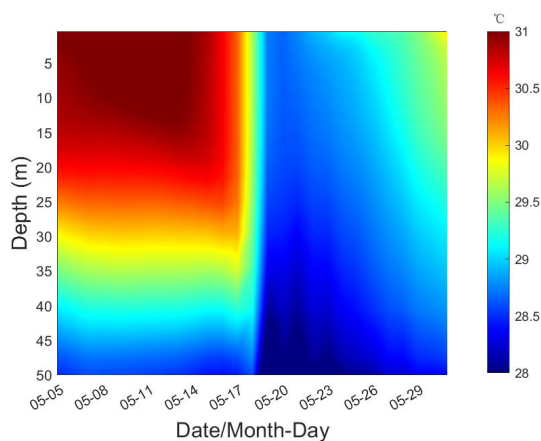


Figure 7. Time series of vertical water temperature from 5 to 31 May in Box A.

that on the northern side reached $-0.199 \text{ mg m}^{-2} \text{ s}^{-1}$. Finally, the surface horizontal transport of Chl *a* rarely changed after 22 May.

3.3 Sea surface height (SSH), current and temperature

The SSH decreased in the southwestern part of Box A, and the southward current increased on 19 May (Fig. 5b). Then, a cyclonic eddy lasting until 3 d after the phytoplankton bloom formed the next day (Fig. 5c and d), both of which are marked by white arrows. The role of the eddy will be discussed in Sect. 4.2.

The averaged TC-induced SST cooling in the Bay of Bengal was studied by Singh and Koll (2022), who noted that the cooling temperature was $2\text{--}3 \text{ }^\circ\text{C}$ ($0.5\text{--}1 \text{ }^\circ\text{C}$) during the pre-monsoon (postmonsoon) season. After the passage of Amphan, the Chl *a* concentration in Box A significantly increased (Fig. 3). Figure 7 shows the vertical distributions of mean temperature from 5 to 31 May in Box A. The lowest SST was $28.6 \text{ }^\circ\text{C}$ in Box A after the passage of Amphan on 20 May. Compared with that on 14 May, the temperature decreased by $2.2 \text{ }^\circ\text{C}$.

3.4 Latent heat flux and tropical cyclone heat potential (TCHP)

During the development of a TC, significant thermal changes will occur near the upper ocean (Liu et al., 2021). From 17 to 20 May, the average latent heat flux in Box A decreased from 250.41 to 96.19 W m^{-2} , and the TCHP had a slight rise and then decreased sharply from 115.28 to 87.16 kJ cm^{-2} (Fig. 6). Moreover, as is vividly shown in Fig. 6i, both the latent heat flux and TCHP reached the lowest values, and after the typhoon made landfall, they rebounded. In total, latent heat fluxes and TCHP correlate with changes in sea surface height because they diminish as the sea level decreases.

3.5 Nitrate distribution

The nitrate concentrations at different depths of $z = -5$, -40 , -50 and -80 m , based on the nitrate climatology data in May, are shown in Fig. 8. Figure 8 clearly shows that high nitrate concentrations were mainly distributed in the north-eastern and southern parts of the Bay of Bengal, and the nitrate concentration in the study area was lower, with a maximum value of $3.8 \mu\text{mol L}^{-1}$ at a depth of 80 m . Poornima et al. (2016) proposed that increased nitrate concentrations promote phytoplankton blooms (Poornima et al., 2016) in the BoB. Although the concentration of nitrate was low in the central BoB, why did the Chl *a* bloom occur in Box A? This will be discussed in Sect. 4.

3.6 Photosynthetically available radiation (PAR)

Figure 9 shows the time series of spatially averaged PAR for Box A. During the passage of Amphan, the PAR had lower values. The cyclone began on 15 May and dissipated on 21 May. The PAR remained at a high level before 15 May and rapidly dropped when the storm formed. On 18 May, when Amphan arrived over the area in Box A, the PAR reached approximately zero, and then it returned to its original state after 21 May when sufficient sunlight entered the euphotic layer, which may have contributed to the Chl *a* bloom on 25 May.

4 Discussion

4.1 The effect of stratification

Generally, ocean stratification has an important effect on the Chl *a* distribution in the upper ocean. The growth of phytoplankton is inversely related to the mixing layer depth. When the mixing layer depth is shallow, an equivalent amount of light intensity will be more helpful for photosynthesis, and when the mixed layer depth is deep, phytoplankton growth will be limited by light intensity, although sufficient nutrients may be available (Niu et al., 2016). Different BLTs in Box A on 8, 18 and 28 May are shown in Fig. 10. The MLD deepened to 39.96 m when Amphan reached Box A (Fig. 10b), which was conducive to Chl *a* entering the upper ocean, and after the passage of Amphan, the MLD became shallower (14.91 m) (Fig. 10c), reaching a depth where the phytoplankton could be influenced by enough PAR.

The barrier layer (BL) plays the role of a barrier in preventing vertical mixing (Balaguru et al., 2012; Sprintall and Tomczak, 1992). As shown in Fig. 10b and c, the BLT became shallower, from 20.03 to 5.17 m , after the passage of the cyclone, which helped uplift Chl *a*. The buoyancy frequencies of Box A on 18 and 28 May are shown in Fig. 11, showing a change from 0.028 to 0.025 s^{-1} . The weakened stratification facilitates the lifting of nutrients below the thermocline to the mixed layer.

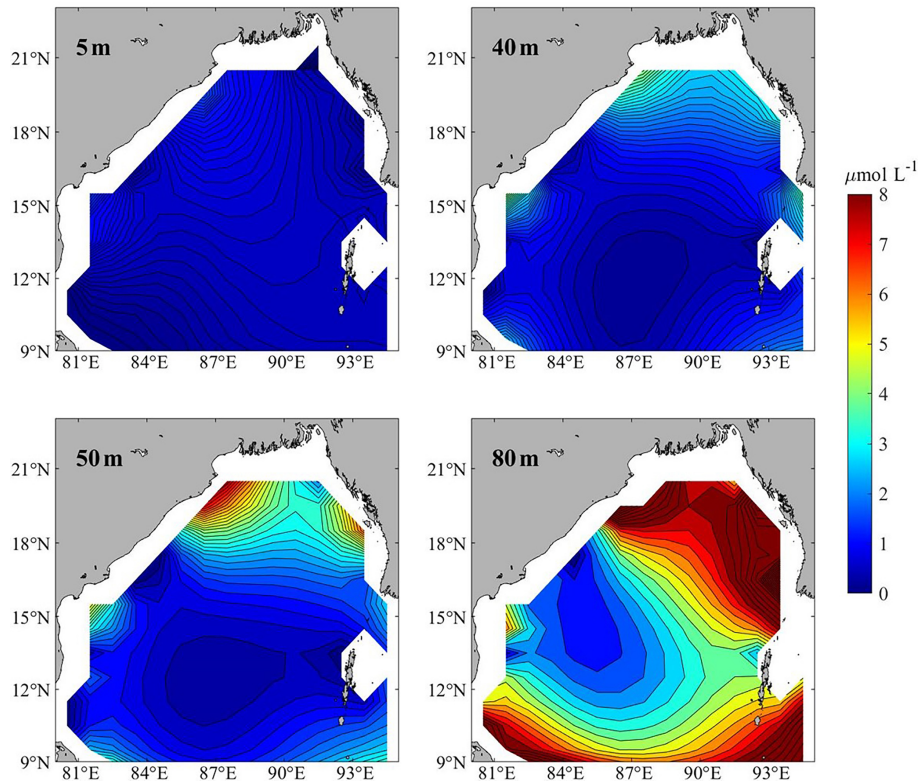


Figure 8. Distribution of nitrate concentration (unit in $\mu\text{mol L}^{-1}$) in May from the WOA.

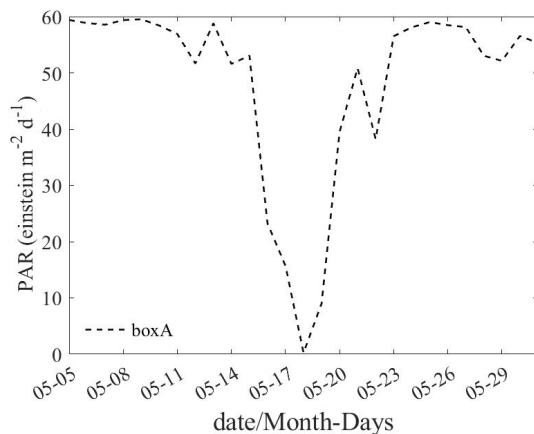


Figure 9. Time series of spatially averaged PAR in Box A from 5 to 31 May.

By means of stratification we can visualize the relationship between Chl *a* flux and thermocline (Qiu et al., 2021), so we divide the upper 100 m into two layers (Fig. 12): above thermocline (0–64 m) and below thermocline (64–100 m). Changes in Chl *a* fluxes above the thermocline were largely consistent with the overall change. The buoyancy frequency weakened to 0.025 s^{-1} , which favored the entry of nutrients from below the thermocline into the mixed layer. Thus, the

Chl *a* fluxes below the thermocline were generally higher than those above the thermocline from 15 to 21 May.

4.2 Effects of the TC and ocean cyclonic eddies

Ekman pumping appears stronger during and after the passage of TCs. Figure 13 shows the EPV during the passage of Amphan. At 12:00 UTC on 18 May 2020, the EPV around the TC center was significantly stronger ($> 5.0 \times 10^{-4} \text{ m s}^{-1}$), and the strong upwelling could bring Chl *a* and nitrate up to the upper-ocean layer.

In order to study the effect of the TC and ocean cyclonic eddies, we quantify the intensity of the cyclonic eddies by calculating the vorticity through Eq. (3). Figure 14c shows the time series of the vertically spatially averaged negative vorticity in Box A from 5 to 31 May. As the TC passed on 19 May, an inertial oscillation with a 2 d cycle period appeared in the thermocline (at a depth of 80 m) and lasted for approximately 2 weeks. At the same time, the latitudinal velocity also changed significantly here (Fig. 14a). This phenomenon was also found in the eastern Arabian Sea during the passage of TCs (Rao et al., 2010). During the passage of Amphan, strong vertical mixing occurred on 19 May, with a maximum vorticity of 0.36 s^{-1} , which transported Chl *a* and nitrate from the deep sea to the upper layer and accounted for the strong upwelling of cold water (Fig. 6). Therefore, it can be proposed that during and after the passage of Am-

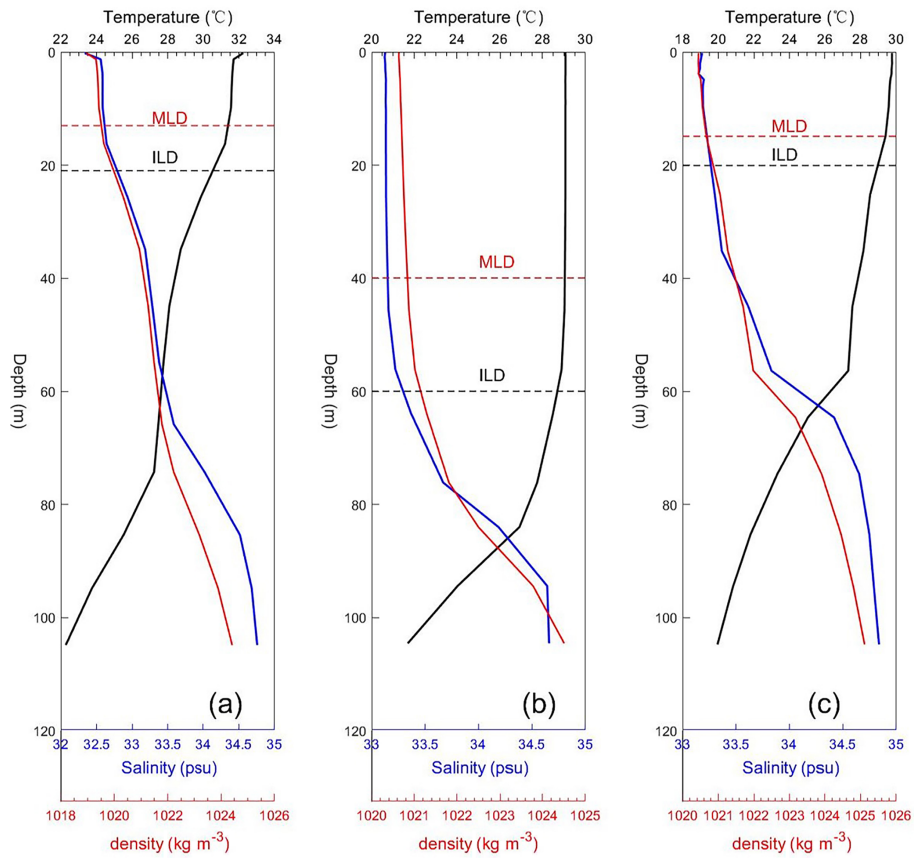


Figure 10. Barrier layer thickness calculated from Argo data in Box A on 8 May (a), 18 May (b) and 28 May (c).

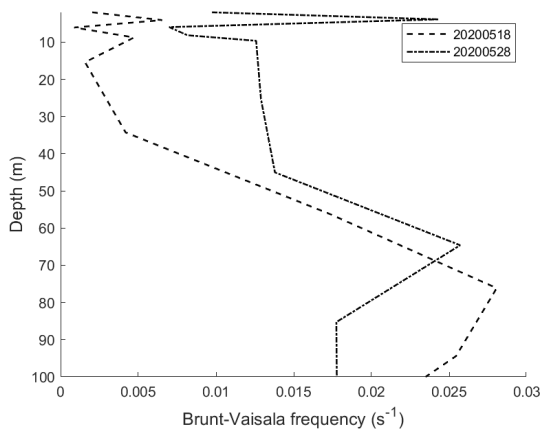


Figure 11. Vertical profile of the buoyancy frequency in Box A from Argo data on 18 and 28 May.

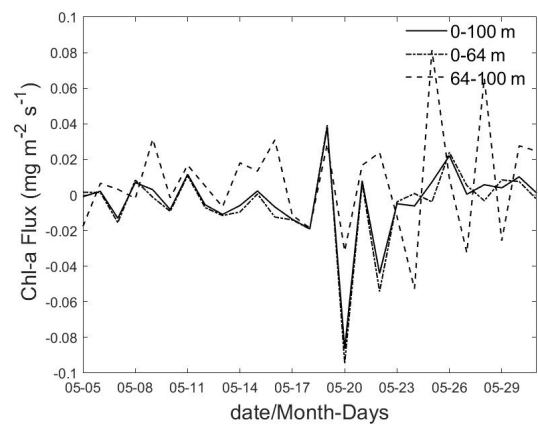


Figure 12. Time series of Chl *a* fluxes through four sides of Box A above the thermocline (0–64 m) and below the thermocline (64–100 m) and for the entire column (0–100 m).

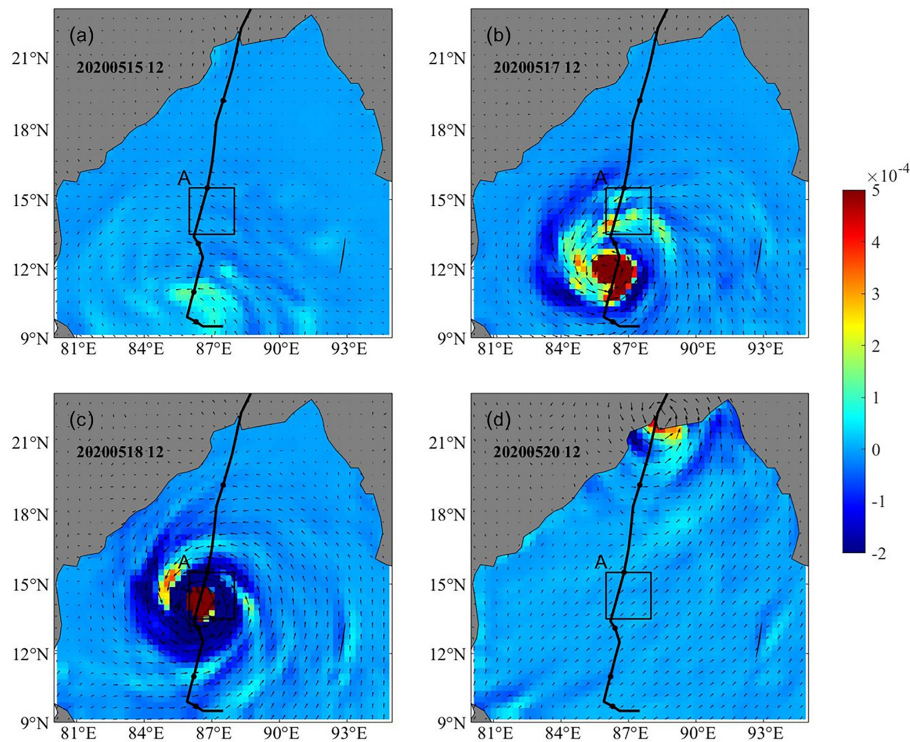


Figure 13. Surface wind speed (arrows) and EPV (colors) during the period time of the TC.

phan, deep water with rich nutrients was transported into the upper ocean through mixing and upwelling, which triggered the surface Chl *a* bloom with the high PAR (Fig. 8).

5 Conclusion

In this study, the dynamic and physical mechanisms of the Chl *a* bloom caused by the super cyclonic storm Amphan in the central Bay of Bengal were investigated by reanalysis data, remote sensing and Argo data, which can provide new insights into the numerical simulation of biological responses in the BoB in the future. The conclusions are as follows:

1. In the study area, there was horizontal transport of Chl *a* in the upper ocean. The maximum inlet flux speed from the western side was $0.304 \text{ mg m}^{-2} \text{ s}^{-1}$, and that of the northern side reached $-0.199 \text{ mg m}^{-2} \text{ s}^{-1}$, which was conducive to the increase in Chl *a* in Box A.
2. After the passage of Amphan, a cyclonic eddy with a high intensity formed in the study area, and a deepened MLD, weakened thermocline and thinner BLT occurred, providing favorable upwelling conditions for the uplift of Chl *a* and nitrate.
3. With high PAR, sufficient nitrate and Chl *a* in the upper layer led to the Chl *a* bloom in the central Bay of Bengal.
4. As the TC passed on 19 May, an inertial oscillation with a 2 d cycle appeared in the thermocline (at a depth of 80 m) and lasted for approximately 2 weeks.

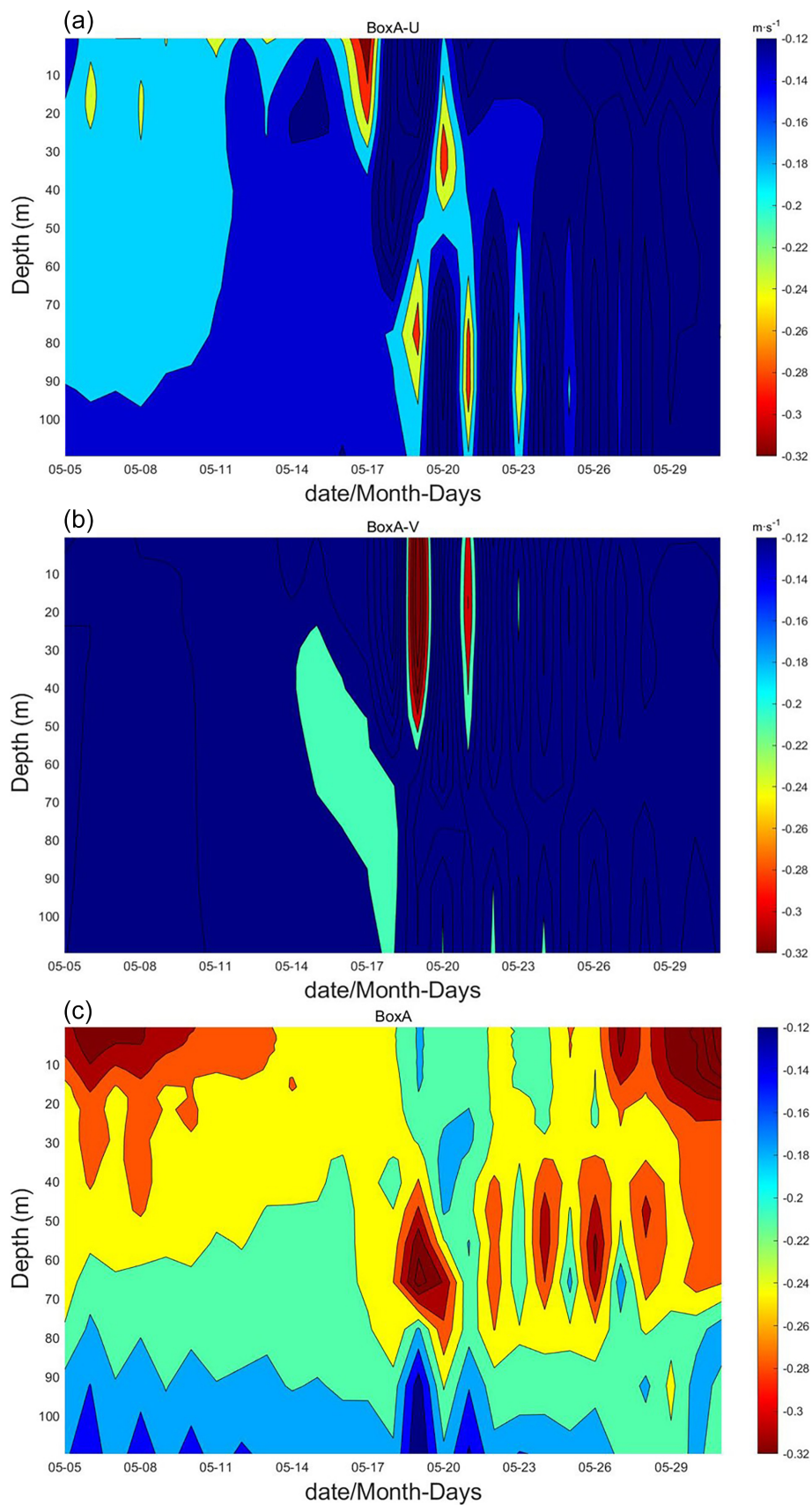


Figure 14. Time series of latitudinal velocity (a), longitudinal velocity (b) and spatially averaged vorticity (c) in Box A from 5 to 31 May.

Data availability. The data used for this research are all from open-access sources listed as follows: Joint Typhoon Warning Center (<https://www.metoc.navy.mil/jtwc/jtwc.html>, Joint Typhoon Warning Center, 2022) for typhoon track data, GlobColour project (<https://www.globcolour.info/>, GlobColour project, 2022) for daily Chl *a* concentration, Copernicus Marine Environment Monitoring Service (<http://marine.copernicus.eu/>, Copernicus Marine Environment Monitoring Service, 2022) for sea current velocity and SSH, Remote Sensing Systems (<https://data.remss.com/>, Remote Sensing Systems, 2022) for SST and wind vector data, Indian Argo project (<http://www.argodatamgt.org/argodamgt>, Indian Argo project, 2022) for the Argo data, and World Ocean Atlas (WOA; <https://www.ncei.noaa.gov/products/world-ocean-atlas>, World Ocean Atlas, 2023) for climatic nitrate data.

Author contributions. Conceptualization: HH and HL; methodology: HH, RW, XD and HL; validation: HS, HH and LB; formal analysis: HH, RW, XD and HL; investigation: HS, HH, LB, RW and XD; data curation: HH, RW, LB and XD; writing – original draft preparation: HH and HL; writing – review and editing: HH and HL; visualization: HS and HH; supervision: HL; project administration: HL; funding acquisition: XD, LB, RW and HL. All authors have read and agreed to the published version of the manuscript.

Competing interests. The contact author has declared that none of the authors has any competing interests.

Disclaimer. Publisher's note: Copernicus Publications remains neutral with regard to jurisdictional claims in published maps and institutional affiliations.

Special issue statement. This article is part of the special issue "Natural hazards' impact on natural and built heritage and infrastructure in urban and rural zones". It is not associated with a conference.

Acknowledgements. We thank Joint Typhoon Warning Center (<https://www.metoc.navy.mil/jtwc/jtwc.html>, last access: 6 September 2022) for typhoon track data, GlobColour project (<https://www.globcolour.info/>, last access: 12 September 2022) for daily Chl *a* concentration, Copernicus Marine Environment Monitoring Service (<http://marine.copernicus.eu/>, last access: 13 September 2022) for sea current velocity and SSH, Remote Sensing (<https://data.remss.com/>, last access: 11 October 2022) for SST, Cross-Calibrated Multi-Platform (CCMP; <http://www.remss.com/measurements/ccmp>, last access: 11 October 2022) for the wind vector data, Indian Argo project (<http://www.argodatamgt.org/argodamgt>, last access: 4 October 2022) for the Argo data, and World Ocean Atlas (WOA; <https://www.ncei.noaa.gov/products/world-ocean-atlas>, last access: 18 February 2023) for climatic nitrate data.

Financial support. This work was funded by the Priority Academic Program Development of Jiangsu Higher Education Institutions (PAPD), Postgraduate Research and Practice Innovation Program of Jiangsu Province (grant no. SJCX22_1657), Postgraduate Research and Practice Innovation Program of Jiangsu Ocean University (grant nos. KYCX2022-29 and KYCX2022-27), Natural Science Foundation of the Jiangsu Higher Education Institutions of China (grant no. 23KJB170005), and National Natural Science Foundation of China (grant no. 62071207).

Review statement. This paper was edited by Maria Bostenaru Dan and reviewed by two anonymous referees.

References

- Akter, N. and Tsuboki, K.: Role of synoptic-scale forcing in cyclogenesis over the Bay of Bengal, *Clim. Dynam.*, 43, 2651–2662, <https://doi.org/10.1007/s00382-014-2077-9>, 2014.
- Bai, L., Lü, H., Huang, H., Muhammad Imran, S., Ding, X., and Zhang, Y.: Effects of Anticyclonic Eddies on the Unique Tropical Storm Deliwe (2014) in the Mozambique Channel, *J. Mar. Sci. Eng.*, 11, 129, <https://doi.org/10.3390/jmse11010129>, 2023.
- Balaguru, K., Chang, P., Saravanan, R., Leung, L. R., Xu, Z., Li, M., and Hsieh, J. S.: Ocean barrier layers' effect on tropical cyclone intensification, *P. Natl. Acad. Sci. USA*, 109, 14343–14347, <https://doi.org/10.1073/pnas.1201364109>, 2012.
- Cai, J., Zhang, Y., Li, Y., Liang, X., and Jiang, T.: Analyzing the Characteristics of Soil Moisture Using GLDAS Data: A Case Study in Eastern China, *Appl. Sci.*, 7, 566, <https://doi.org/10.3390/app7060566>, 2017.
- Cheung, H.-F., Pan, J., Gu, Y., and Wang, Z.: Remote-sensing observation of ocean responses to Typhoon Lupit in the northwest Pacific, *Int. J. Remote Sens.*, 34, 1478–1491, <https://doi.org/10.1080/01431161.2012.721940>, 2012.
- Copernicus Marine Environment Monitoring Service: <http://marine.copernicus.eu/> (last access: 13 September 2022).
- Dwivedi, R. M., Raman, M., Babu, K. N., Singh, S. K., Vyas, N. K., and Matondkar, S. G. P.: Formation of algal bloom in the northern Arabian Sea deep waters during January–March: a study using pooled in situ and satellite data, *Int. J. Remote Sens.*, 29, 4537–4551, <https://doi.org/10.1080/01431160802029693>, 2008.
- Gaube, P., Chelton, D. B., Strutton, P. G., and Behrenfeld, M. J.: Satellite observations of chlorophyll, phytoplankton biomass, and Ekman pumping in nonlinear mesoscale eddies, *J. Geophys. Res.-Oceans*, 118, 6349–6370, <https://doi.org/10.1002/2013jc009027>, 2013.
- Girishkumar, M. S. and Ravichandran, M.: The influences of ENSO on tropical cyclone activity in the Bay of Bengal during October–December, *J. Geophys. Res.-Oceans*, 117, C02033, <https://doi.org/10.1029/2011jc007417>, 2012.
- GlobColour project: <https://www.globcolour.info/> (last access: 12 September 2022), 2022.
- Golder, M. R., Shuva, M. S. H., Rouf, M. A., Uddin, M. M., Bristy, S. K., and Bir, J.: Chlorophyll-*a*, SST and particulate organic carbon in response to the cyclone Amphan in the Bay of Bengal, *J. Earth Syst. Sci.*, 130, 157, <https://doi.org/10.1007/s12040-021-01668-1>, 2021.

- Gomes, H. R., Goes, J. I., and Saino, T.: Influence of physical processes and freshwater discharge on the seasonality of phytoplankton regime in the Bay of Bengal, *Cont. Shelf Res.*, 20, 313–330, [https://doi.org/10.1016/s0278-4343\(99\)00072-2](https://doi.org/10.1016/s0278-4343(99)00072-2), 2000.
- Gould, W. J.: From Swallow floats to Argo – the development of neutrally buoyant floats, *Deep-Sea Res. Pt. II*, 52, 529–543, <https://doi.org/10.1016/j.dsr2.2004.12.005>, 2005.
- Guan, M.: An Effective Method for Submarine Buried Pipeline Detection via Multi-Sensor Data Fusion, *IEEE Access.*, 7, 125300–125309, <https://doi.org/10.1109/ACCESS.2019.2938264>, 2019.
- He, Q., Zhan, H., and Cai, S.: Anticyclonic eddies enhance the winter barrier layer and surface cooling in the Bay of Bengal, *J. Geophys. Res.-Oceans*, 125, e2020JC016524, <https://doi.org/10.1029/2020JC016524>, 2020.
- Indian Argo project: <http://www.argodatamgt.org/argodamgt/> (last access: 4 October 2022), 2022.
- Jayne, S., Roemmich, D., Zilberman, N., Riser, S., Johnson, K., Johnson, G., and Piotrowicz, S.: The Argo Program: Present and Future, *Oceanography*, 30, 18–28, <https://doi.org/10.5670/oceanog.2017.213>, 2017.
- Joint Typhoon Warning Center: <https://www.metoc.navy.mil/jtwc/jtwc.html> (last access: 6 September 2022), 2022.
- Liu, Y., Lu, H., Zhang, H., Cui, Y., and Xing, X.: Effects of ocean eddies on the tropical storm Roanu intensity in the Bay of Bengal, *PLoS One*, 16, e0247521, <https://doi.org/10.1371/journal.pone.0247521>, 2021.
- Lu, H., Zhao, X., Sun, J., Zha, G., Xi, J., and Cai, S.: A case study of a phytoplankton bloom triggered by a tropical cyclone and cyclonic eddies, *PLoS One*, 15, e0230394, <https://doi.org/10.1371/journal.pone.0230394>, 2020.
- Lü, H., Xie, J., Xu, J., Chen, Z., Liu, T., and Cai, S.: Force and torque exerted by internal solitary waves in background parabolic current on cylindrical tendon leg by numerical simulation, *Ocean Eng.*, 114, 250–258, <https://doi.org/10.1016/j.oceaneng.2016.01.028>, 2016.
- Mitra, A.: Amphan Supercyclone: A death knell for Indian Sundarbans, *J. Appl. Forest Ecol.*, 8, 41–48, 2020.
- Nayak, S. R. and Rajawat, A. S.: Application of IRS-P4 OCM data to study the impact of cyclone on coastal environment of Orissa, *Curr. Sci.*, 80, 1208–1213, 2001.
- Niu, L., van Gelder, P. H. A. J. M., Zhang, C., Guan, Y., and Vrieling, J. K.: Physical control of phytoplankton bloom development in the coastal waters of Jiangsu (China), *Ecol. Model.*, 321, 75–83, <https://doi.org/10.1016/j.ecolmodel.2015.10.008>, 2016.
- Nyadjro, E. S., Wang, Z., Reagan, J., Cebrian, J., and Shriver, J. F.: Bio-Physical Changes in the Gulf of Mexico During the 2018 Hurricane Michael, *IEEE Geosci. Remote Sens. Lett.*, 19, 1–5, <https://doi.org/10.1109/lgrs.2021.3068600>, 2022.
- Poornima, D., Shanthi, R., Ranith, R., Senthilnathan, L., Sarangi, R. K., Thangaradjou, T., and Chauhan, P.: Application of in-situ sensors (SUNA and thermal logger) in fine tuning the nitrate model of the Bay of Bengal, *Remote Sens. Appl.: Soc. Environ.*, 4, 9–17, <https://doi.org/10.1016/j.rsase.2016.04.002>, 2016.
- Qiu, G., Xing, X., Chai, F., Yan, X.-H., Liu, Z., and Wang, H.: Far-Field Impacts of a Super Typhoon on Upper Ocean Phytoplankton Dynamics, *Front. Mar. Sci.*, 8, 643608, <https://doi.org/10.3389/fmars.2021.643608>, 2021.
- Qiu, Z.: Dam Structure Deformation Monitoring by GB-InSAR Approach, *IEEE Access.*, 8, 123287–123296, <https://doi.org/10.1109/ACCESS.2020.3005343>, 2020.
- Rao, A. D., Joshi, M., Jain, I., and Ravichandran, M.: Response of subsurface waters in the eastern Arabian Sea to tropical cyclones, *Estuar. Coast. Shelf Sci.*, 89, 267–276, <https://doi.org/10.1016/j.ecss.2010.07.011>, 2010.
- Rao, K. H., Smitha, A., and Ali, M. M.: A study on cyclone induced productivity in south-western Bay of Bengal during November–December 2000 using MODIS (SST and chlorophyll-*a*) and altimeter sea surface height observations, *Indian J. Geo-Mar. Sci.*, 35, 153–160, 2006.
- Remote Sensing Systems: Remote Sensing Systems for SST and wind vector data, <https://data.remss.com/> (last access: 16 August 2023), 2022.
- Roemmich, D., Johnson, G., Riser, S., Davis, R., Gilson, J., Owens, W. B., Garzoli, S., Schmid, C., and Ignaszewski, M.: The Argo Program: Observing the Global Oceans with Profiling Floats, *Oceanography*, 22, 34–43, <https://doi.org/10.5670/oceanog.2009.36>, 2009.
- Singh, V. and Koll, R.: A review of the ocean-atmosphere interactions during tropical cyclones in the north Indian Ocean.pdf, *Earth-Sci. Rev.*, 226, 103967, <https://doi.org/10.1016/j.earscirev.2022.103967>, 2022.
- Sprintall, J. and Tomczak, M.: Evidence of the barrier layer in the surface layer of the tropics, *J. Geophys. Res.*, 97, 7305–7316, <https://doi.org/10.1029/92jc00407>, 1992.
- Thadathil, P., Muraleedharan, P. M., Rao, R. R., Somayajulu, Y. K., Reddy, G. V., and Revichandran, C.: Observed seasonal variability of barrier layer in the Bay of Bengal, *J. Geophys. Res.*, 112, C02009, <https://doi.org/10.1029/2006jc003651>, 2007.
- Vinayachandran, P. N.: Phytoplankton bloom in the Bay of Bengal during the northeast monsoon and its intensification by cyclones, *Geophys. Res. Lett.*, 30, 1572, <https://doi.org/10.1029/2002gl016717>, 2003.
- Wang, J., Tang, D., and Sui, Y.: Winter phytoplankton bloom induced by subsurface upwelling and mixed layer entrainment southwest of Luzon Strait, *J. Mar. Syst.*, 83, 141–149, <https://doi.org/10.1016/j.jmarsys.2010.05.006>, 2010.
- World Ocean Atlas: <https://www.ncei.noaa.gov/products/world-ocean-atlas> (last access: 18 February 2023, 2023).
- Xia, C., Ge, X., Lü, H., Zhang, H., Xing, X., and Cui, Y.: A phytoplankton bloom with a cyclonic eddy enhanced by the tropical cyclone Phethai in eastern Sri Lanka, *Reg. Stud. Mar. Sci.*, 51, 102217, <https://doi.org/10.1016/j.rsma.2022.102217>, 2022.
- Zhao, H., Tang, D., and Wang, D.: Phytoplankton blooms near the Pearl River Estuary induced by Typhoon Nuri, *J. Geophys. Res.*, 114, C12027, <https://doi.org/10.1029/2009jc005384>, 2009.
- Zhao, H., Shao, J., Han, G., Yang, D., and Lv, J.: Influence of Typhoon Matsa on Phytoplankton Chlorophyll-*a* off East China, *PLoS One*, 10, e0137863, <https://doi.org/10.1371/journal.pone.0137863>, 2015.